npj | climate and atmospheric science

Article

Published in partnership with CECCR at King Abdulaziz University

https://doi.org/10.1038/s41612-025-01224-4

Synoptic systems influence the effectiveness of spectral nudging in high-resolution simulations of extreme precipitation

Daeun Kwon[1], Ga-Yeong Seo[1], Seung-Ki Min[1,2] ✉, Seok-Woo Son[3], Young-Hee Ryu[1,4], Eun-Soon Im[5,6], Dong-Hyun Cha[7], Jin-Uk Kim[8], Young-Hwa Byun[8] & Kyung-On Boo[8]

Spectral nudging (SN) is an effective numerical technique that prevents the background field from deviating excessively from the boundary conditions in regional climate modeling. This study investigates the effectiveness of SN in convection-permitting model simulations of three typical events of warm-season extreme precipitation in South Korea. The case studies show that SN improves extreme precipitation simulations by keeping synoptic circulations more consistent with observations. Trajectory analysis also shows that SN influences the moisture transport and local ascent that trigger extreme precipitation. However, the extent of the improvement depends on the synoptic condition and the domain size. The influence of SN generally increases with increasing domain size, especially for events driven by the developing upper-level trough with strong baroclinic instability compared to those influenced by surface processes. SN is also found to be more effective in events whose dominant wave scales fall between the domain size and the cut-off wavelength used for SN. Based on a series of sensitivity experiments, it is proposed that the most effective configuration for simulating extreme precipitation events is to apply SN to a domain approximately 3000 km wide.

Extreme precipitation events have a profound impact on human society, leading to catastrophic flooding, which is often accompanied by loss of life and destruction of property. In South Korea, extreme precipitation has been ranked as the second leading cause of fatalities and the primary cause of financial losses among natural disasters in the past decades[1]. Therefore, research to improve the understanding and prediction of extreme precipitation is imperative. Extreme precipitation events that occur in mid-latitude regions, including South Korea, originate from multi-scale weather systems. The major types include tropical cyclones (TCs), extratropical cyclones (ETCs), and local or mesoscale convection[2–5]. Each type of extreme precipitation event has regional and seasonal characteristics[6,7].

Extreme precipitation events in East Asia occur mainly during the warm-season owing to the influence of the East Asian summer monsoon and TCs. Precipitation types not directly connected with TCs account for approximately 80% of the extreme precipitation on a sub-daily scale[8]. Park et al.[7] reported that such extreme precipitation mostly involves transient ETCs and the quasi-stationary front. The ETC is an important synoptic weather system in the mid-latitudes as it facilitates the poleward transport of heat and momentum and is often accompanied by heavy precipitation and strong surface winds[9–11]. Although ETCs exhibit diverse characteristics, some travel along the front while others propagate as relatively isolated features, they are generally associated with baroclinic instability and a moisture-rich environment[12–14]. Similar environmental conditions can be observed during extreme precipitation events that do not involve ETCs. These include abrupt surface low development and moisture pathway, formed by remote effect of TCs or local convective instability, between large-scale continental and oceanic highs, and extreme precipitation events occurring at local scale[15].

[1]Division of Environmental Science and Engineering, Pohang University of Science and Technology, Pohang, South Korea. [2]Institute for Convergence Research and Education in Advanced Technology, Yonsei University, Seoul, South Korea. [3]School of Earth and Environmental Sciences, Seoul National University, Seoul, South Korea. [4]Department of Atmospheric Sciences, Yonsei University, Seoul, South Korea. [5]Department of Civil and Environmental Engineering, The Hong Kong University of Science and Technology, Hong Kong SAR, China. [6]Division of Environment and Sustainability, The Hong Kong University of Science and Technology, Hong Kong SAR, China. [7]Department of Civil Urban Earth and Environmental Engineering, Ulsan National Institute of Science and Technology, Ulsan, South Korea. [8]Climate Change Research Team, National Institute of Meteorological Sciences, Jeju, South Korea. ✉e-mail: skmin@postech.ac.kr

Such complex extreme precipitation events have been observed in South Korea and various methodologies have been employed to study them. A rapid development of extreme precipitation has often been investigated using high-resolution regional climate model (RCM). High-resolution RCM is particularly useful for studying extreme precipitation events on a regional scale[16,17]. Researchers also use it to examine the characteristics and projected changes in extreme precipitation under various climate scenarios, including future warming and counterfactual non-warming conditions[18–20]. In such modeling, spectral nudging (SN) has been widely used to prevent the model background flows from deviating from the boundary conditions[21,22]. This approach involves the retention of circulation at wavelengths longer than a specified threshold, thereby bringing the large-scale circulations in the model closer to the observations[23,24]. However, the nudging variables and coefficients used in SN are often chosen subjectively[25–27]. The optimal domain size for SN is also uncertain, although the size and location of the domain influence the simulation performance. In general, as the domain size increases, the influence of lateral boundary conditions becomes more dispersed, while the internal model dynamics and physical parameterization become more pronounced[28,29].

Given the significance of SN in regional climate modeling, this study aims to investigate its effects on the simulation of extreme precipitation events in South Korea. To address this research objective, series of sensitivity experiments are carried out for three extreme precipitation events with different background synoptic conditions. Those extreme events, named according to the year and month of occurrence, are listed in Table S1. Briefly, the 202108 event is characterized by the expanded Western North Pacific Subtropical High (WNPSH) and an upper-level trough and its westward tilt are indications of baroclinicity (Fig. 1a). This event is accompanied by strong moisture transport along a quasi-stationary front between the transient ETC in the northwest and the WNPSH in the southeast (Fig. 1b). The 202007 event is caused by a strong ETC traveling eastward from eastern China. During this event, a well-defined circular low pressure developed (Fig. 1c). Unlike the 202108 event, this event was characterized by strong moisture transport by the ETC itself (Fig. 1d). The 201009 event developed between continental and oceanic highs without a synoptic-scale ETC (Fig. 1e). A narrow, zonally oriented, and intense moisture transport is organized along the surface front (Fig. 1f). According to a self-organizing map clustering analysis[7,30], the selected extreme events cover approximately 45% of warm-season extreme precipitation events in South Korea that are not directly associated with TCs, making them reasonable cases for studying the target region and season. The 202108 event is classified as a heavy rainfall event caused by a local disturbance at the edge of the WNPSH, the 202007 event is classified as an extratropical cyclone originating from eastern China, and the 201009 event is classified as an event associated with a moisture pathway between continental and oceanic highs.

The sensitivity experiment is designed to analyze how the effects of SN depend on the synoptic condition of extreme precipitation events and the domain size. Experiments are conducted with and without SN, denoted ON and OFF, respectively. Three different domain sizes (Fig. S1), from Domain1 to Domain3, are also considered. These experiments, labeled D1_ON, D1_OFF, D2_ON, D2_OFF, D3_ON and D3_OFF, are conducted for three extreme precipitation events with five ensemble members (see Methods). The results are analyzed in terms of model performance in capturing the observed precipitation features. Not only the location and intensity of extreme precipitation but also the synoptic conditions such as moisture transport, ETC, and vertical coupling with the upper-level potential vorticity (PV) are investigated in detail to explore how the SN-induced improvement occurs.

Results

Spatial and temporal distribution of hourly precipitation

SN evidently improves the spatial distribution of hourly precipitation in the 202108 and 202007 events, with its impact increasing as the domain size expands (Fig. 2a–p). In contrast, in the 201009 event, the influence of SN is relatively negligible compared to the other two events (Fig. 2q–x).

For the 202108 event, two precipitation cores are observed: one inland to the north and one offshore to the south (Fig. 2a, b). The core relevant to the event is the southern one. In the ON experiments, the core is situated inland in all domain simulations (Fig. 2c, e, g), whereas it is not inland in the OFF experiments with wide domains (Fig. 2d, f). The 202007 event exhibits

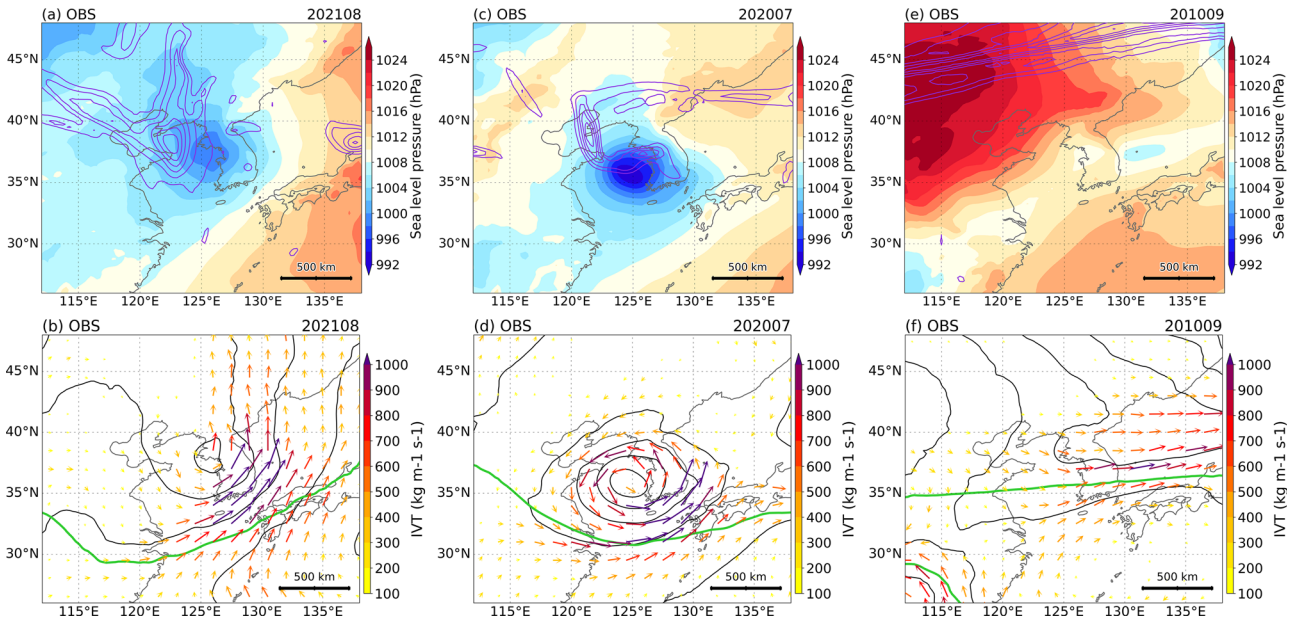

Fig. 1 | Synoptic conditions of selected extreme precipitation events. **a**, **b** correspond to the 202108 event, **c**, **d** to the 202007 event, and **e**, **f** to the 201009 event. For each event, the first row (**a**, **c**, **e**) depicts the surface and upper-level dynamic features, where the purple contour represents 300 hPa potential vorticity, and the shading indicates the mean sea level pressure. The second row (**b**, **d**, **f**) illustrates the moisture transport and mid-to lower-level features. Vectors represent integrated vapor transport (IVT), black contours indicate 850 hPa geopotential height, and green contours highlight the 5880 m geopotential height at 500 hPa, marking the extent of the Northwest Pacific Subtropical High. All panels correspond to the time of maximum observed hourly precipitation recorded at the surface stations for each event.

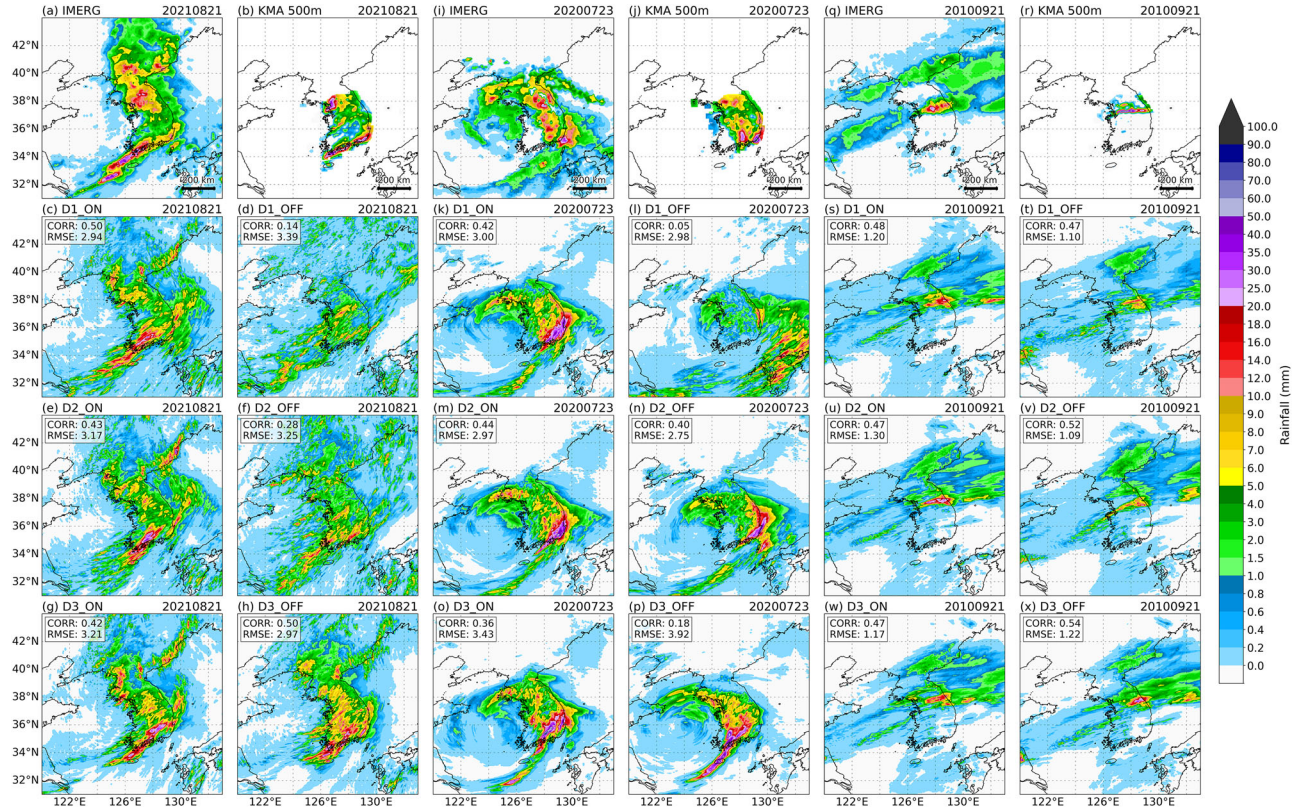

Fig. 2 | Spatial distribution of hourly precipitation at the time of maximum hourly precipitation observed at surface stations for each event. a–h correspond to the 202108 event, **i–p** to the 202007 event, and **q–x** to the 201009 event. The first row in each event (**a–b**, **i–j**, **q–r**) represents observational data derived from IMERG and KMA 500 m datasets. The second to fourth rows show the model experimental results. In the model panels, the left column (**c**, **e**, **g**, **k**, **m**, **o**, **s**, **u**, **w**) presents the results from simulations with spectral nudging, whereas the right column (**d**, **f**, **h**, **l**, **n**, **p**, **t**, **v**, **x**) presents the results without spectral nudging. All model results represent the ensemble mean values. Spatial correlation coefficient (CORR) and root mean square error (RMSE) are indicated for each experiment, which were calculated using IMERG dataset. The model experimental results are re-gridded to match the spatial resolution of IMERG before calculating CORR and RMSE.

a precipitation core to the right of the ETC center in the observations, which corresponds to the location of ETC-induced strong moisture transport[31,32] (Fig. 2i, j). Therefore, the 202007 event is representative of the importance of properly simulating the location and intensity of ETCs during extreme precipitation. In the ON experiments, the position of the ETC center is simulated to be similar to the observation in all domains (Fig. 2k, m, o). However, in the OFF experiments, the position of the ETC center slightly shifts (Fig. 2l, n, p). For the 201009 event, the influence of SN on the precipitation core simulations is less pronounced than in the previous two events. This event showed a localized precipitation core and a zonally-elongated shape of the precipitation band in the observations (Fig. 2q, r), which is well represented in all experiments (Fig. 2s–x).

SN enhances the model performance in the hourly peak simulations for the 202108 and 202007 events (Fig. 3a–n), whereas the influence of SN is relatively less pronounced in the 201009 event (Fig. 3o–u). In the formers, SN contributes to making the magnitude and timing of the hourly peak simulation closer to the observations. Without SN, the ensemble spread is larger, and it increases further with domain size, indicating a reduced influence of lateral boundary conditions in a larger domain. In cases where the SN effect is not prominent, the influence of the domain size is also relatively small.

The 202108 event exhibits a single peak in the observed time series (Fig. 3a). All model experiments underestimate the magnitude of the peak, with the OFF experiments showing greater underestimation in Domain1 and Domain2 (Fig. 3b–g). This result can be interpreted as SN assisting in reducing ensemble spread by constraining large-scale background conditions. The ON experiment simulates the peak timing more accurately in Domain2 (Fig. 3d, e), whereas no noticeable difference in timing between ON and OFF experiments is shown in Domain1 and Domain3 (Fig. 3b, c, f, g). The 202007 event shows multiple peaks in the observed time series (Fig. 3h), with a later peak occurring at the targeted peak time. In this event, the model simulations do not significantly underestimate the peak magnitude. Similar to the 202108 event, the ensemble spread is wider in the OFF experiments, becoming more evident with larger domains. The 201009 event displays a preceding weak peak followed by a more pronounced peak later in the observed time series (Fig. 3o). The latter peak is the chosen event, and all model experiments substantially underestimate its intensity, although they simulate the timing of the peak similar to the observation (Fig. 3p–u). Unlike other events, there are minimal differences among the model experiments with narrower ensemble spreads, indicating that the impact of SN is not evident in the 201009 event.

Relationship between moisture transport and precipitation

We found that the performance enhancement by SN in precipitation simulations varies across different experiments. Here, we analyze how the same SN configuration results in different effects depending on the event and domain size. It is well known that the Integrated Vapor Transport (IVT) is strongly linked to extreme hourly precipitation. Intense IVT is crucial for extreme precipitation as it indicates moisture source and contributes to convective instability at lower atmospheric levels. In South Korea, regions that experience heavy rainfall frequently coincide with areas of intense moisture transport[33–35]. IVT is also closely associated with transient ETCs. Zhang et al.[36] examined the relationship between ETCs and atmospheric rivers and found that atmospheric rivers are prone to form in the warm conveyor belt of the ETC structure. They also showed that while the location of maximum IVT is related to the ETC center, it has large variability. Their

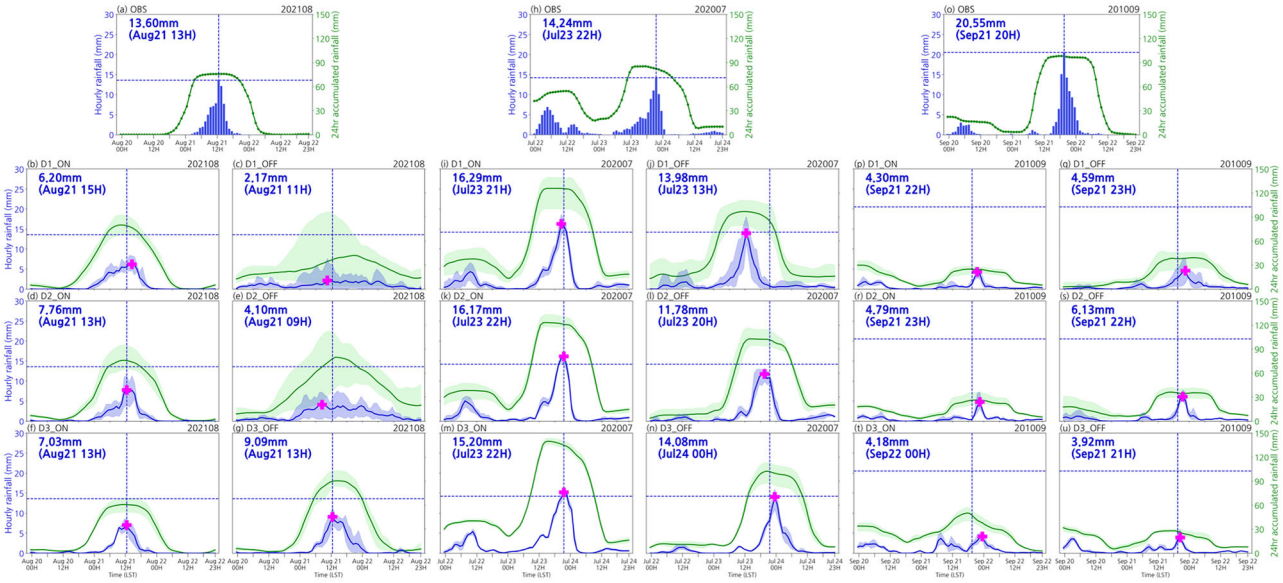

Fig. 3 | Time series of spatially averaged precipitation. The averaging domain for each event is defined by the grid points where the observed hourly precipitation exceeded 5 mm at the time of maximum hourly precipitation recorded at the surface stations. **a**–**g** correspond to the 202108 event, **h**–**n** to the 202007 event, and **o**–**u** to the 201009 event. The first row (**a**, **h**, **o**) represents the observational data derived from the KMA 500 m dataset. The second to fourth rows show the model experimental results. In the model panels, the left column (**b**, **d**, **f**, **i**, **k**, **m**, **p**, **r**, **t**) presents results from simulations with spectral nudging, whereas the right column (**c**, **e**, **g**, **j**, **l**, **n**, **q**, **s**, **u**) presents results without spectral nudging. In the observational data panels, the blue bars represent hourly precipitation, and the green line indicates 24-h accumulated precipitation. The blue dotted line marks the timing (x-axis) and magnitude (y-axis) of the maximum observed hourly precipitation, and its value is displayed in the upper-left text. In the model panels, the pink marker indicates the timing and magnitude of maximum hourly precipitation in the model simulation. The shading represents the range of ensemble members in the model results.

results align with the analysis by Park et al.[33], which suggested that IVT formation can be directly induced by ETCs in some cases, while in others, it is primarily governed by large-scale systems.

The selected events consistently demonstrate strong IVT in regions with high hourly precipitation across both observations and all simulations (Fig. S2). In the 202108 event, an intense IVT is induced by large-scale pressure systems, while a transient cyclone system contributes to its enhancement as it moves through the region (Fig. S2a). During the 202007 event, the intense IVT was mainly generated by the ETC itself, rather than large-scale conditions (Fig. S2h). In the 202108 and 202007 events, where SN significantly impacts precipitation simulations, SN is also effective in simulating both the position and intensity of IVT, particularly in larger domains, bringing the results closer to the observations (Figs. S2a–g; S2h–n). Conversely, in the 201009 event, its effect on the IVT simulation is minimal similar to its impact on the precipitation simulation (Fig. S2o–u). Also, a TC feature is observed near the South China Sea in the 201009 event. Although the TC near the South China Sea does not appear in the Domain3 experiment results due to the limited domain area, the strong IVT over the Korean Peninsula, which is associated with the extreme precipitation event, is well represented.

In order to examine the relationship between the IVT and cyclone system, the trajectories of the ETC center and related IVT center are analyzed (Fig. 4). The observational trajectory results show ETC and IVT centers move together during all events, and SN appears effective at constraining their positions. In most experiments, the ON experiments show smaller error distances compared to the OFF experiments (Table 1, Fig. 5). SN proves effective in the 202108 and 202007 events, while its influence is less evident in the 201009 event based on the precipitation evaluation. Despite the presence of a few outlier ensemble members in the OFF experiment for the 201009 event (Fig. 5c), the trajectory analysis supports this finding (Table 1). As the domain size increases, the effect of SN becomes more pronounced in most experiments. The ensemble spread tends to widen with increasing domain size in the OFF experiments, but the impact of SN outweighs the domain size effect. The 202108 event is characterized by the ETC and IVT advancement from southwest to northeast along the boundary of the WNPSH (Fig. 4a–g). The IVT center is located to the south of the ETC center, which is consistent with the structure of the warm conveyor belt of the ETC. In most experiments, this event exhibits the greatest error distance, with largest improvement due to SN (Table 1). In the 202007 event, the ETC and IVT centers propagate eastward, with the IVT center positions south of the ETC center, similar to the 202108 event (Fig. 4h–n). As the domain size increases in Domain1 and Domain2, the effect of SN strengthens. However, between Domain2 and Domain3, the effect of SN is slightly greater in Domain3. The 201009 event has a smaller spatial scale compared to the other events (Fig. 4o). Eastward propagating ETC and IVT centers are observed, and the IVT center is located to the south of the ETC center. The detected trajectories in the model show that the ETC and IVT centers are located closer than observations. Moreover, the trajectories are generally biased toward the north in all experiments (Fig. 4p–u).

Impact of upper-level conditions on the extreme precipitation

The investigation into the connection between IVT and precipitation, as well as the association between the cyclone system and IVT, confirms their association. Based on these findings, we further examined how SN influences IVT and the cyclone system, both of which play a crucial role in precipitation events. Specifically, SN is applied above the planetary boundary layer (PBL) in this study (see Methods), which is usually utilized to reduce bias in upper-to-mid troposphere[37,38]. Thus, we assessed the upper-level potential vorticity (PV), eddy geopotential height and jet streak (Fig. S3). The eddy geopotential height is calculated for each dataset by subtracting the corresponding zonal mean (110–150°E) geopotential height to analyze the relative pressure condition. The positive PV and eddy geopotential height represent the upper-level trough of the cyclone system in the 202108 event (Fig. S3a). This upper-level trough exhibits a westward tilt as altitude increases, reflecting the baroclinic instability structure of the precipitation system. SN contributes to simulating the position and intensity of this trough more accurately. In the case of the jet, the streak adjacent to the western boundary of the domain exhibits only limited influence from SN,

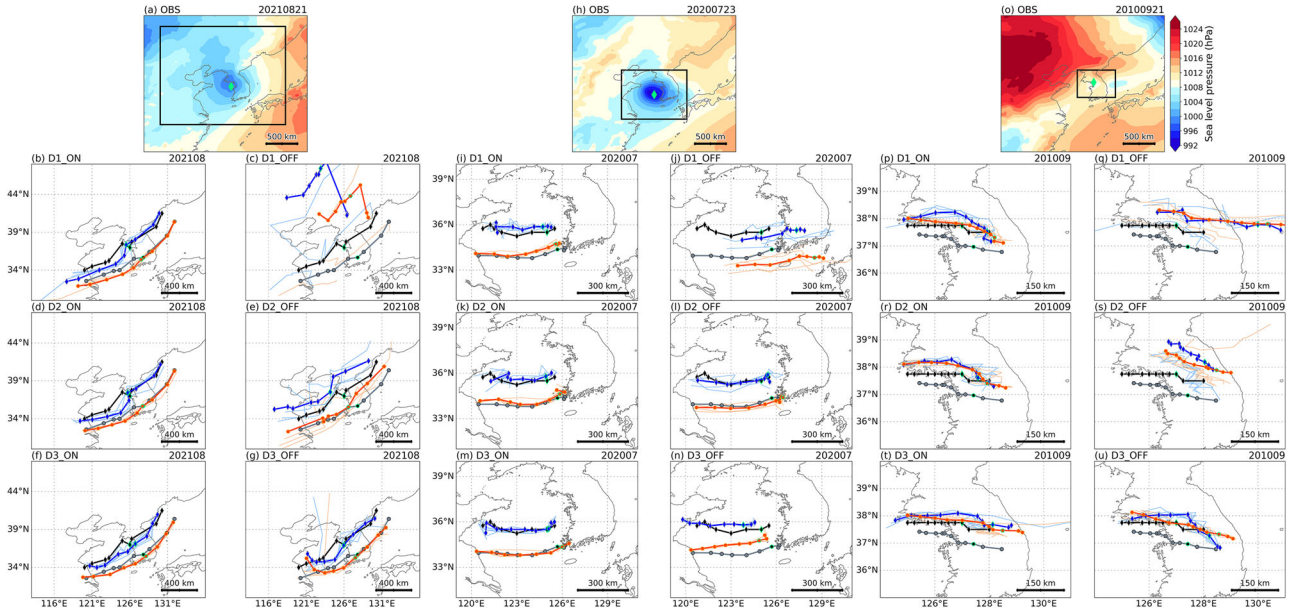

Fig. 4 | Spatial distribution of mean sea level pressure (MSLP) and trajectories of the extratropical cyclone (ETC) and integrated vapor transport (IVT) center. **a**–**g** correspond to the 202108 event, **h**–**n** to the 202007 event, and **o**–**u** to the 201009 event. The first row (**a**, **h**, **o**) presents MSLP from observational data at the time of the maximum hourly precipitation recorded at the surface stations. ERA5 reanalysis data is used for all observational panels. The second to fourth rows present the trajectories detected in both the observation and the model simulations. In the trajectory panels, the left column (**b**, **d**, **f**, **i**, **k**, **m**, **p**, **r**, **t**) presents results of simulations with spectral nudging, whereas the right column (**c**, **e**, **g**, **j**, **l**, **n**, **q**, **s**, **u**) presents results without spectral nudging. In the observational MSLP panels, the black rectangles indicate the area where the trajectory is detected in each case, and the green diamonds mark the local minima of MSLP within this area. In the trajectory panels, the black and gray lines represent the observed ETC and IVT center trajectories, respectively. The thick blue and orange lines indicate the ensemble mean trajectories of the ETC and IVT center, respectively. The thin blue and orange lines denote the trajectories of individual ensemble members. The green-bordered markers indicate the position of the ETC and IVT center at the time of maximum hourly precipitation observed. The values in parentheses in the legend display the distance between the observation and ensemble mean trajectories at the time of maximum hourly precipitation. The marker interval is 3-h for the 202108 and 202007 events and 1-h for the 201009 event.

Table 1 | Comparison of distance errors in simulated center trajectories of ETC and IVT

Experiment	202108		202007		201009	
Center of trajectory	ETC	IVT	ETC	IVT	ETC	IVT
D1_ON	123.01	88.16	49.14	40.35	71.32	74.52
D1_OFF	954.26	781.94	282.37	291.85	201.01	207.14
Difference	−831.25	−693.78	−233.23	−251.50	−129.69	−132.62
D2_ON	76.30	48.05	52.81	36.52	66.99	85.32
D2_OFF	236.52	116.72	85.67	61.21	136.51	140.77
Difference	−160.22	−68.67	−32.86	−24.69	−69.52	−55.45
D3_ON	98.55	73.96	35.21	23.16	76.82	92.85
D3_OFF	109.54	106.86	83.48	78.90	93.25	87.56
Difference	−10.99	−32.90	−48.27	−55.74	−16.43	+5.29

Distances (km) between observed and ensemble mean ETC and IVT center trajectories during the analysis period are provided for three domains (D1, D2, and D3) together with their differences between ON and OFF experiments (ON – OFF). Refer to Fig. 5 for the error distance distribution across ensemble members.

whereas the jet located east of the trough is relatively more affected by the SN (Fig. S3b–g). It is likely due to the strong influence of lateral boundary conditions near the western boundary of the domain, which masks the effects of SN. Consequently, further inside the domain, the jet streak is also affected by SN along with PV. The upper-level divergence at the jet exit and the resulting low-pressure and upward motion enhancement is a well-known dynamical structure of heavy precipitation events in mid-latitudes[39–41]. In this event, the relationship between the jet streak and the cyclone trough indicates favorable condition for upward motion. In the 202007 event, an upper trough and baroclinic instability structure are also observed (Fig. S3h). The shape of the trough and jet in D1_ON resemble those in the observations, whereas there are deviations in D1_OFF experiment (Fig. S3i, j). In Domain2 and Domain3, the influence of SN is not apparent in the upper-level synoptic condition (Fig. S3k–n). The jet streak intensity is also affected by the domain size, with stronger jet streaks in smaller domains. In the 201009 event, a zonal and strong upper-level jet is observed over the Korean Peninsula with a PV streak to its north (Fig. S3o). Such strong upper-level positive PV, as observed in the 202108 and 201009 events, is occasionally associated with stratospheric high-PV intrusions[42,43]. When strong meridional PV gradients develop in the upper troposphere, jet stream tends to form along regions where a positive PV anomaly is present on the poleward side and a negative anomaly on the equatorward side[44,45]. These characteristics are well simulated in all model experiments, and the impact of SN is not distinctly noticeable (Fig. S3p–u).

The differences in upper troposphere conditions induced by SN affect the mid- and lower-level troposphere (Fig. 6). In the 202108 and 202007

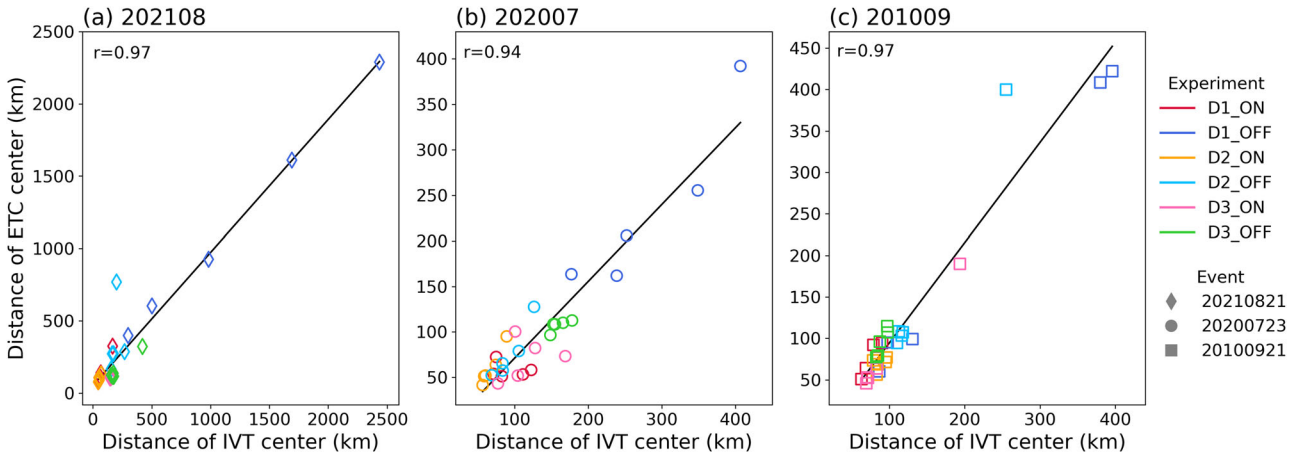

Fig. 5 | Relationship between error distance of ETC and IVT center. Scatter plots of error distance of ETC and IVT center. Distance represents the mean difference between the observed and simulated trajectories from each ensemble, as shown in Fig. 4. **a** corresponds to the 202108 event, **b** to the 202007 event, and **c** to the 201009 event. The marker shape indicates the event, and the color represents the experiment. Each experiment includes five ensemble members. The correlation coefficient (r) is calculated using the entire ensemble for each event.

events, SN influences the upper-level trough, which is typically accompanied by strong positive PV. The deepening of PV can be interpreted as contributing to the intensification of surface cyclones through baroclinic instability[32], by enhancing the vertical extension of the trough from the upper to the mid-levels and modifying the horizontal gradient of potential temperature (Fig. 6a–n). As a result, the synoptic-scale vertical structure, the location of intense IVT, and the position and intensity of ascent driven by dynamic (upper-level large-scale trough) and diabatic (lower-level latent heating) forcings[46,47] are affected by SN. These changes subsequently lead to differences in precipitation simulations. In contrast, for cases like the 201009 event, where the upper-level conditions do not primarily drive the synoptic-scale vertical structure and precipitation, the impact of SN in the RCM simulations is reduced (Fig. 6o–u).

In the 202108 event, observations clearly show the deepening of the upper-level trough and the associated baroclinic vertical structure. Strong upward motion and IVT on the eastern side of the trough create favorable conditions for extreme precipitation (Fig. 6a). SN contributes to maintaining this baroclinic vertical structure within the model, simulating the location and intensity of precipitation closer to the observation. This effect becomes more significant as the domain size increases (Fig. 6b–g). Similarly, in the 202007 event, strong upward motion and IVT are present in the eastern regions of baroclinic instability structure. SN helps anchor these features consistent with observations (Fig. 6h, i, k, m). In contrast, in the large domain experiment without SN (D1_OFF, D2_OFF), shifts occur in the location of baroclinic instability, IVT peaks, and the resulting upward motion (Fig. 5j, l, n). In the 201009 event, while upward motion is present from the surface to mid-level, along with intense IVT at the near location, no distinct connection is present between upper-level dynamics and these favorable precipitation conditions (Fig. 6o). This suggests that the extreme precipitation of the 201009 event is more affected by surface trough and baroclinicity development, rather than the dynamic forcing from the upper-level synoptic pattern, despite the presence of upper-level jet streak and weak trough[7]. As a result, the influence of SN is less pronounced (Fig. 6p–u).

We further define a deep PV intensity metric to quantitatively assess the relationship between the influence of SN on the baroclinic instability and precipitation simulation (Fig. S4). The deep PV intensity is examined for the two events (202108 and 201009) where the connection of the vertical atmospheric structure and precipitation is evident. The analysis reveals that SN contributes to a stronger and more realistic representation of the deepening of positive PV, which subsequently improves the simulation of the ETC center trajectories. The ETC center is also closely related to the IVT center (Fig. 5). In summary, the interaction between SN and IVT, eventually hourly precipitation, does not occur directly but rather through SN restricting the upper-level trough.

Role of domain size on SN effectiveness

Our analysis has identified the influence of domain size on the simulation of hourly precipitation, extratropical cyclones, and IVT. We further investigate the underlying mechanisms responsible for the differing impacts of domain size across the events. A power spectrum analysis is conducted for 500 hPa geopotential height anomalies to evaluate the horizontal scale dependence on SN effectiveness (Fig. 7). We assume that SN would be more effective when the dominant wave scale is contained within the domain and exceeds the cut-off wavelength for SN, approximately 1000 km. It corresponds to the Rossby raidus of deformation in troposphere of midlatitude, setting the transition from the synoptic scale to the convective scale[48,49]. For both the 202108 and 202007 events, power spectrum is strong within the wavelength ranges spanning from the SN cut-off wavelength to the widths of Domain1 and Domain2, indicating that SN effectively constrains synoptic-scale Rossby waves (Fig. 7d, h). As a result, the D1_ON and D2_ON experiments show superior performance in simulating the intensity and position of the trough near 125°E (Fig. 7a, b, e, f). In contrast, the ON and OFF experiments show minimal differences in Domain 3, with particularly negligible discrepancies in the 202108 event (Fig. 7c, g). It is challenging for Domain3 to capture typical synoptic-scale Rossby waves, approximately 2000–3000 km in wavelength[50], due to the narrow zonal extent. Although SN is applied in this domain experiment, its impact on Rossby waves is expected to be limited. Unlike the other events, 201009 event exhibits relatively weak power spectrum within the wavelength bands that can be resolved within the given experimental domains (Fig. 7l). This suggests that the limitation of SN results from the scale mismatch between the zonal wave scale of the event and the domain size. Furthermore, the 202007 and 201009 events involve a wider spectrum of wave scales than the 202108 event, which may explain the overall reduction in power spectrum observed in these events.

Discussion

The sensitivity experiments show that SN makes the simulations of extreme precipitation more consistent with observations. In particular, the application of SN improves the location and intensity of the upper-level trough, which in turn contributes to a more realistic simulation of the baroclinic structure in the mid-troposphere and related surface cyclone. It affects the moisture transport, responsible for the extreme precipitation. Through this process, SN influences not only dynamical processes but also thermodynamic processes of diabatic ascent and

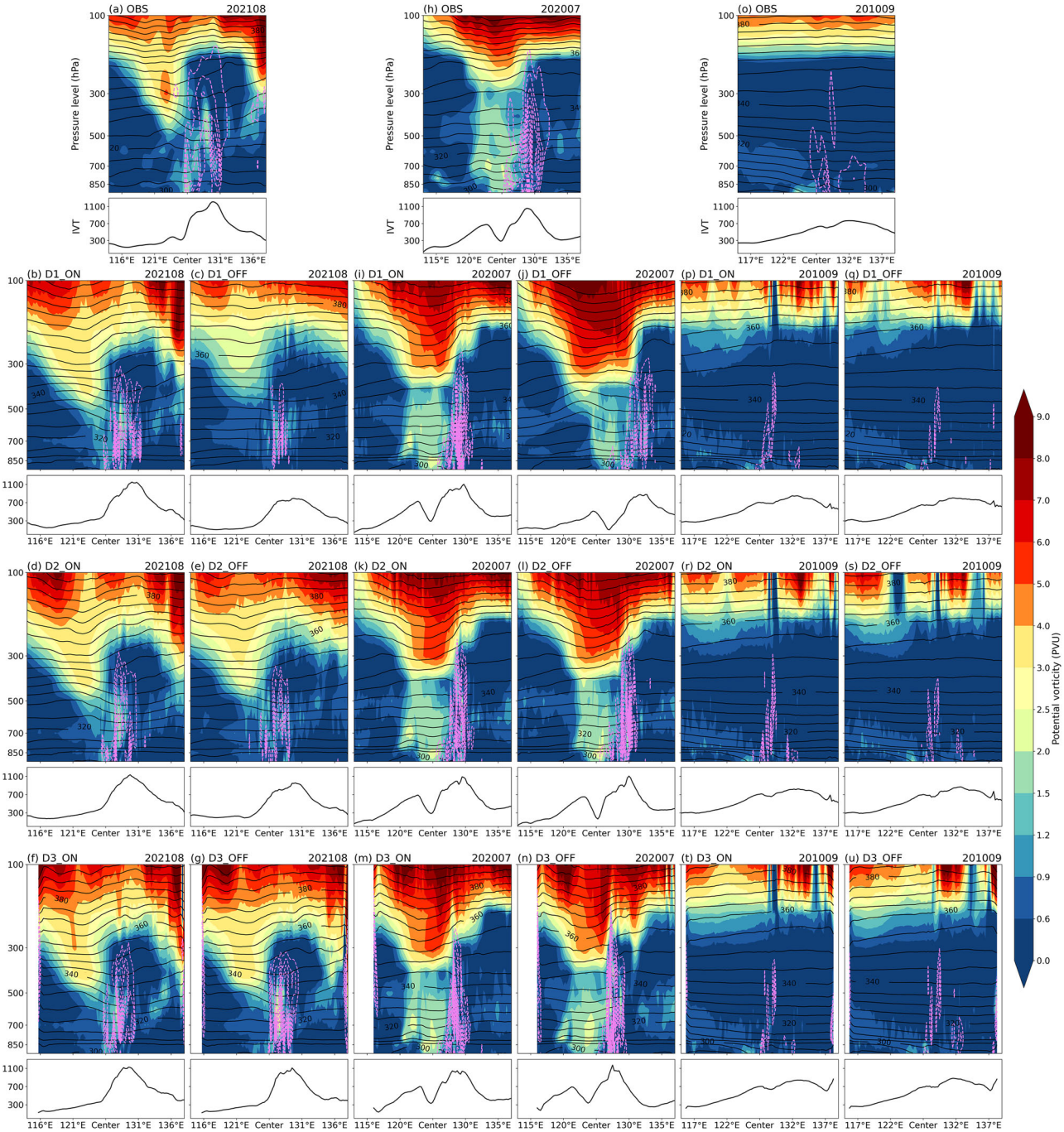

Fig. 6 | Zonal cross-section of potential vorticity (PV), potential temperature (θ), vertical pressure velocity (ω), and meridionally averaged magnitude of integrated vapor transport (IVT). Panels **a**-**g** correspond to the 202108 event, **h**-**n** to the 202007 event, and **o**-**u** to the 201009 event. The first row (**a, h, o**) represents the observational data. The second to fourth rows show the model experimental results. In the model panels, the left column (**b, d, f, i, k, m, p, r, t**) presents results from simulations with spectral nudging, whereas the right column (**c, e, g, j, l, n, q, s, u**) presents results without spectral nudging. In each panel, the top plot shows a zonal-vertical cross-section of PV, θ, and ω. The shading represents PV, black contours indicate θ, and pink contours denote negative ω, with a contour interval of 0.25 Pa s^{-1}. The bottom plot illustrates the meridionally averaged magnitude of IVT. All panels correspond to the time of maximum observed hourly precipitation at the surface stations for each event. The meridional averaging range for both the cross-section and IVT magnitude plots extended by ±2° in latitude from the ETC center.

atmospheric moisture that triggers extreme precipitation, although it only nudged horizontal winds above PBL, not temperature and humidity. The improvement of SN generally increases with increasing model domain size. In smaller domains, synoptic-scale waves are not sufficiently resolved in the simulation and the influence of lateral boundary conditions increases. However, its effect varies from event to event. Therefore, the alignment between the dominant horizontal wave scale of the event and the domain size also has a significant influence.

The performance improvement by SN is significant in the 202108 and 202007 events where the upper-level trough plays a crucial role. In contrast, the SN has a limited influence on the simulation of the 201009 event. This event is not driven by a synoptic-scale ETC Instead, the abrupt development of the surface trough and baroclinicity is more primarily attributed to the generation of the moisture pathway than to upper-level dynamics. Moreover, the 202108 and 202007 events are primarily influenced by synoptic-scale waves that are well captured within the experimental domains, whereas

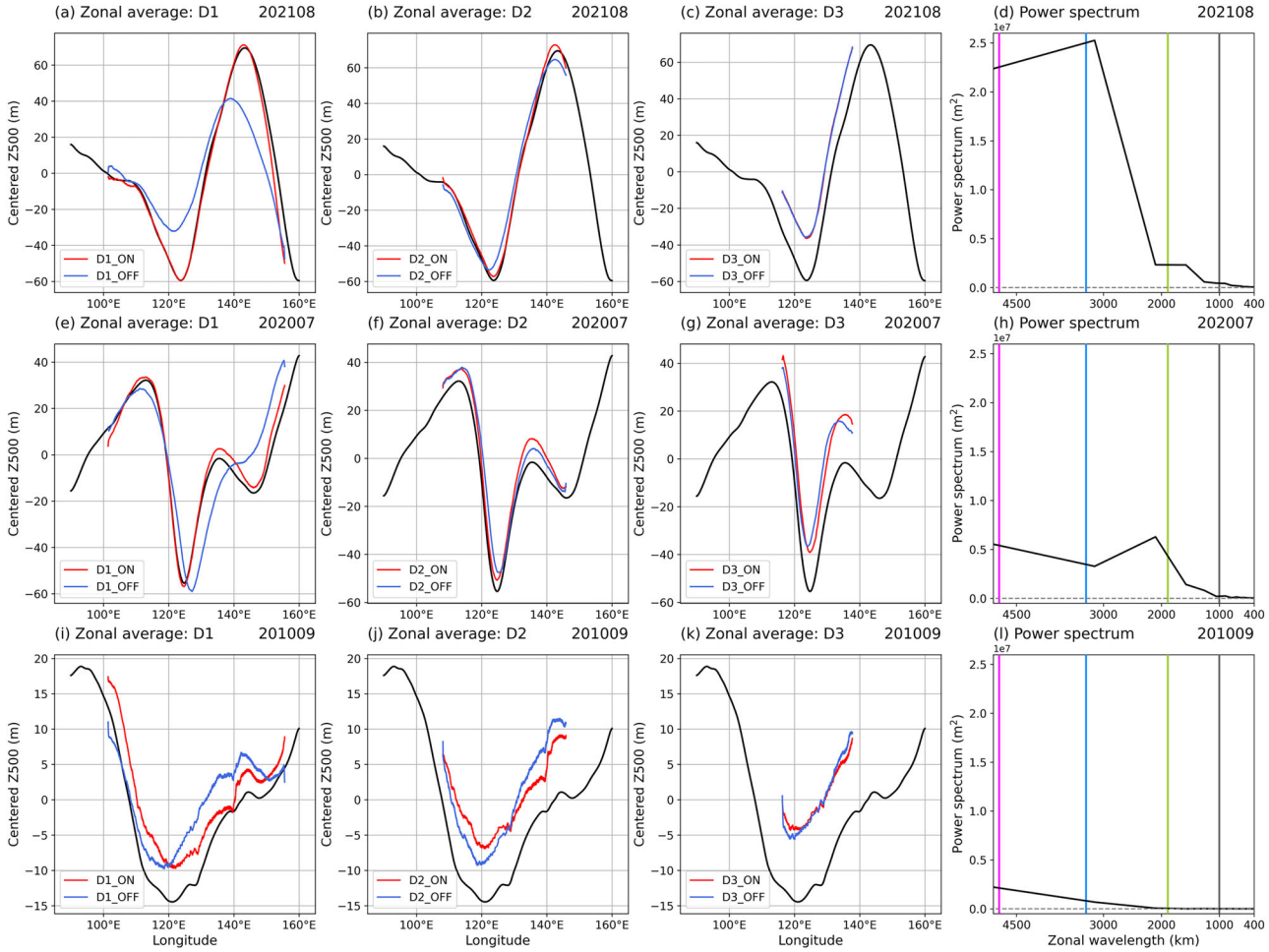

Fig. 7 | 500 hPa geopotential height anomalies and power spectrum analysis. **a**–**d** correspond to the 202108 event, **e**–**h** to the 202007 event, and **i**–**l** to the 201009 event. For each event, the first to the third columns show (**a**–**c**, **e**–**g**, **i**–**k**) the latitude-band (29°N–43°N) averaged anomalies of 500 hPa geopotential height for each domain. The black lines represent the observed results. The red and blue lines indicate the model simulation results with and without spectral nudging, respectively. The averaging period is ±3-h centered on the time of maximum hourly precipitation observed at surface stations for each event. Anomalies are obtained by subtracting the zonal mean. All model results represent ensemble mean values. The rightmost columns (**d**, **h**, **l**) present the results of the power spectrum analysis of the geopotential height anomalies obtained from using Fast Fourier Transform. The pink, blue, and green vertical lines indicate the widths of the Domain1, Domain2 and Domain3, respectively. The gray dashed line shows the red noise power spectrum.

the 201009 event is triggered by mesoscale disturbances embedded within a larger-scale background flow. In summary, the results of this study reveal that SN has a greater impact on extreme precipitation events driven by the upper-level trough and strong baroclinic instability than in those influenced by surface processes. Its influence is also more pronounced in events whose zonal scales lie between the domain size and the threshold wavelength of SN. Moreover, SN generally contributes to more realistic simulations and reduced ensemble spread. However, its effect can vary depending on the event and domain size, especially when the influence of SN is limited.

Practically, within the scope of the specific cases and experimental design of the study, the D2_ON configuration is proposed as the most efficient option for simulating extreme precipitation events where SN is effective (e.g., the 202108 and 202007 events). The regional climate simulation with small domain size degrades the representation of the large-scale features and internal model dynamics due to a lack of spin-up distance for boundary forcing, whereas excessively large domains can lead to strong deviations of the simulation from its lateral boundary conditions[28,51,52]. In our experiments, the domains that adequately cover the major synoptic-scale zonal waves of events sensitive to SN are Domain1 and Domain2 (Fig. 7). We determined that Domain2 would be more efficient and reasonable than Domain1, as Domain1 includes an abrupt topographical feature on its western boundary due to the Tibetan Plateau[53,54] and considering the high horizontal resolution, the computational cost would have been too expensive.

This study quantitatively analyzed the impact of SN on extreme precipitation simulations events. Unlike previous studies, more comprehensive and mechanism-based analyses were conducted by considering both synoptic characteristics and domain size. This approach enables a more detailed understanding of how SN can be optimized for different types of extreme precipitation events and domain sizes. There are still areas for improvement, suggesting that further research could build upon the present study to refine the understanding and application of SN in high-resolution modeling. First, further investigation is necessary to validate the consistency of the results across multiple events for each type of extreme precipitation. The reliance of this study on a single representative event for each type may limit the generalizability of its results. Second, the model physics schemes affect precipitation simulations using RCM, with microphysics and PBL schemes being particularly important in convection-permitting simulations[55–57]. In East Asian precipitation simulations, the microphysics scheme significantly influences the hourly maximum precipitation, as different schemes represent and classify hydrometeors (e.g., ice, rain, snow, graupel) in distinct ways, directly affecting the formation and intensity of precipitation particles. The PBL scheme exerts strong control over the average accumulated precipitation by modulating vertical mixing and the

turbulent transport of heat and moisture in the lower atmosphere[58]. This interdependence highlights the need for a more thorough investigation of how different model configurations interact with SN techniques.

We also applied SN to hindcast the events, but further research is required to investigate the impact of nudging on forecast fields or global climate models to simulate extreme precipitation[45]. In addition, the development of quantitative guidelines regarding the horizontal scale and vertical structure of extreme precipitation systems with respect to significant SN effects would be a valuable contribution to the field. Such guidelines could enhance the use of high-resolution models in extreme precipitation research, potentially improving the accuracy and reliability of the simulations.

Methods

Data

The European Center for Medium-Range Weather Forecasts reanalysis fifth generation (ERA5) was used as synoptic observation data and initial and lateral boundary forcing for model simulations[59]. For model evaluation, we utilized two observational datasets of the spatial distribution of precipitation. High-resolution gridded data from Korea Meteorological Administration (KMA 500 m) is a dataset generated by applying a three-dimensional objective analysis technique to assimilate various station observations while incorporating terrain effects[60]. Integrated Multi-Satellite Retrievals for Global Precipitation Measurement (IMERG) is a NASA product that estimates global surface precipitation rates at a high resolution of 0.1° every half-hour, beginning in 2000[61]. Instead of high spatial resolution KMA 500 m data, which is only available for the South Korean land area, IMERG offers a wide cover area with relatively lower resolution. Thus, both KMA 500 m and IMERG were used to evaluate the spatial distribution of precipitation (Fig. 2), and KMA 500 m data were used to evaluate the time series of precipitation (Fig. 3).

Model configuration

The Weather Research and Forecasting (WRF) model version 4.4 is employed in this study. The WRF model has a single domain with a 3 km horizontal resolution. Based on this high-resolution, we conducted a convection-permitting simulation that explicitly resolves precipitation using microphysics parameterization instead of convection parameterization[62–64]. For the sensitivity experiment, we designed SN and the domain settings. The theoretical basis of the SN option in WRF model version 4.4 is consistent with that of the default SN scheme, in which atmospheric waves longer than the specified cut-off wavenumber are nudged toward the reference values derived from the lateral boundary conditions[21,22,65]. SN is applied above PBL with coefficient of 3×10^{-4}. The nudged wavenumber varies slightly across domains, with a filtering applied to wavelengths longer than approximately 1000 km for each domain (Table S2). We configure the nudging to assimilate only the horizontal wind components (u, v wind), as previous studies[66,67] have shown that this approach is sufficient for effective improvement while simplifying the nudging setup. The cut-off wavelength is selected to constrain synoptic patterns and preserve the internal dynamics of the fine scale model[49]. A coefficient of 3×10^{-4} s^{-1} was used to apply nudging on an hourly basis. The domain settings are as follows: the largest domain (Domain1) covers the South China Sea and the WNPSH; the second largest domain (Domain2) includes the Yangtze River and WNPSH; and the smallest domain (Domain3) encompasses the Korean Peninsula (Fig. S1). The approximate width of each domain is 4500 km for Domain1, 3000 km for Domain2 and 1800 km for Domain3. The sensitivity experiment consists of six combinations in total, involving the application of SN (ON) and the non-application of SN (OFF) for each domain. The experiment was conducted for three selected events, resulting in eighteen simulations in total. To construct ensemble members, each simulation was performed five times, with the initialization time for each run delayed by 6-hour intervals from the start of the simulation period. Further details of the model configurations are provided in Table S2 of the Supporting Information.

Tracking method

The following methods are utilized in this study to obtain the ETC and IVT center trajectories. First, the trajectory of the ETC center is detected using the approach suggested by Coll-Hidalgo et al.[68]. First, we prefiltered potential centers in the mean sea level pressure (MSLP) field as locations where the difference between the current MSLP and the average over the previous 5 days is lower than −3 hPa. The point with the lowest MSLP value is selected as the cyclone center. In the next time step, we identify the points where the anomaly below −3 hPa using the same method, but within a restricted radius around the ETC center of previous time step. Among these points, the one with the lowest MSLP value is designated as the ETC center for the next time step. The timestep interval (3-h for 202108 and 202007; 1-hfor 201009) and restricted radius (500 km for 202108 and 202007; 100 km for 201009) are selected based on the spatial scale of each event. The tracking period is set to include the time of maximum hourly precipitation observed.

The IVT center is determined as the central point of the IVT pattern associated with the ETC center. First, the IVT pattern is determined by the area exceeding a IVT magnitude threshold within a specified radius around the ETC center (500 km for 202108 and 202007; 300 km for 201009). The IVT magnitude threshold is defined individually for each observation and ensemble member. It is set as the 85th percentile of IVT magnitudes that exceed 100 kg m^{-1} s^{-1} within the trajectory analysis domain during the two-day period before and after the event date. The 85th percentile was chosen as a reference because it has been used in previous research to define strong and corridor-shaped IVT, the atmospheric river[69–71]. Then, the central point position of the IVT pattern is calculated as the mean latitude and longitude values of the grid points within the IVT pattern. The latitude and longitude are weight-averaged based on the IVT values corresponding to each grid point.

Data availability

Coupled Model Inter-comparison Project Phase 6 data can be downloaded from the Earth System Grid Federation (ESGF) MetaGrid. ERA5 hourly data are available from the Copernicus Climate Data Store[72]. IMERG half-hourly precipitation data is accessible via the Goddard Earth Sciences Data and Information Services Center (GES DISC)[61]. High-resolution gridded data from the Korea Meteorological Administration (KMA) is accessible via the KMA Application Programming Interface (API) Hub service[60].

Code availability

The code used in this study will be provided upon a reasonable request.

Received: 26 May 2025; Accepted: 3 September 2025;
Published online: 10 October 2025

References

1. Ministry of the Interior and Safety. 2023 Natural Disaster Yearbook (in Korean). *Open Government Data Portal.* https://www.data.go.kr/data/15016405/fileData.do# (2024).
2. Kunkel, K. E. et al. Meteorological causes of the secular variations in observed extreme precipitation events for the conterminous United States. *J. Hydrometeorol.* **13**, 1131–1141 (2012).
3. Vellore, R. K. et al. Monsoon-extratropical circulation interactions in Himalayan extreme rainfall. *Clim. Dyn.* **46**, 3517–3546 (2016).
4. Li, P. et al. Mesoscale convective system precipitation characteristics over East Asia. part I: regional differences and seasonal variations. *J. Clim.* **33**, 9271–9286 (2020).
5. Prein, A. F., Mooney, P. A. & Done, J. M. The multi-scale interactions of atmospheric phenomenon in mean and extreme precipitation. *Earth's Fut.* **11**, e2023EF003534 (2023).
6. Jo, E. et al. Classification of localized heavy rainfall events in South Korea. *Asia Pac. J. Atmos. Sci.* **56**, 77–88 (2020).
7. Park, C. et al. Diverse synoptic weather patterns of warm-season heavy rainfall events in South Korea. *Monthly Weather Rev.* **149**, 3875–3893 (2021).

8. Utsumi, N., Kim, H., Kanae, S. & Oki, T. Relative contributions of weather systems to mean and extreme global precipitation. *J. Geophys. Res. Atmos.* **122**, 152–167 (2017).
9. Hartmann, D. L. *Global physical climatology* (Newnes, 2015).
10. Hawcroft, M., Shaffrey, L., Hodges, K. & Dacre, H. How much Northern Hemisphere precipitation is associated with extratropical cyclones? *Geophys. Res. Lett.* **39**, L24809 (2012).
11. Kang, J. M., Lee, J., Son, S. W., Kim, J. & Chen, D. The rapid intensification of East Asian cyclones around the Korean Peninsula and their surface impacts. *J. Geophys. Res. Atmos.* **125**, e2019JD031632 (2020).
12. Song, H.-J. & Sohn, B.-J. Two heavy rainfall types over the Korean peninsula in the humid East Asian summer environment: a satellite observation study. *Monthly Weather Rev.* **143**, 363–382 (2015).
13. Lee, J. et al. Extratropical cyclones over East Asia: climatology, seasonal cycle, and long-term trend. *Clim. Dyn.* **54**, 1131–1144 (2020).
14. Yang, G. & Li, T. Moist Baroclinic Instability along the Subtropical Mei-Yu Front. *J. Clim.* **36**, 805–822 (2023).
15. Shibuya, R., Takayabu, Y. & Kamahori, H. Dynamics of widespread extreme precipitation events and the associated large-scale environment using AMeDAS and JRA-55 Data. *J. Clim.* **34**, 8955–8970 (2021).
16. Lee, D., et al. Enhanced role of convection in future hourly rainfall extremes over South Korea. *Geophys. Res. Lett.* **49**, e2022GL099727 (2022).
17. Sun, X. et al. An evaluation of dynamical downscaling of Central Plains summer precipitation using a WRF-based regional climate model at a convection-permitting 4 km resolution. *J. Geophys. Res. Atmos.* **121**, 13,801–813,825 (2016).
18. Kendon, E. J. et al. Do Convection-Permitting Regional Climate Models Improve Projections of Future Precipitation Change?. *Bull. Am. Meteorol. Soc.* **98**, 79–93 (2017).
19. Fowler, H. J. et al. Anthropogenic intensification of short-duration rainfall extremes. *Nat. Rev. Earth Environ.* **2**, 107–122 (2021).
20. Wang, J. et al. Storyline attribution of human influence on a record-breaking spatially compounding flood-heat event. *Sci. Adv.* **9**, eadi2714 (2023).
21. von Storch, H., Langenberg, H. & Feser, F. A spectral nudging technique for dynamical downscaling purposes. *Monthly Weather Rev.* **128**, 3664–3673 (2000).
22. Miguez-Macho, G., Stenchikov, G. L. & Robock, A. Spectral nudging to eliminate the effects of domain position and geometry in regional climate model simulations. *J. Geophys. Res. Atmos.* **109**, D13104 (2004).
23. Tang, J. et al. Impact of spectral nudging on regional climate simulation over CORDEX East Asia using WRF. *Clim. Dyn.* **48**, 2339–2357 (2017).
24. Huang, Z., Zhong, L., Ma, Y. & Fu, Y. Development and evaluation of spectral nudging strategy for the simulation of summer precipitation over the Tibetan Plateau using WRF (v4.0). *Geosci. Model Dev.* **14**, 2827–2841 (2021).
25. Ma, Y. et al. Comparison of analysis and spectral nudging techniques for dynamical downscaling with the WRF model over China. *Adv. Meteorol.* **2016**, 4761513 (2016).
26. Mai, X., Qiu, X., Yang, Y. & Ma, Y. Impacts of spectral nudging parameters on dynamical downscaling in summer over mainland China. *Front. Earth Sci.* **8**, 574754 (2020).
27. Tang, J. et al. Effects of spectral nudging on precipitation extremes and diurnal cycle over CORDEX-East Asia domain. *Int. J. Climatol.* **38**, 4903–4923 (2018).
28. Seth, A. & Giorgi, F. The effects of domain choice on summer precipitation simulation and sensitivity in a regional climate model. *J. Clim.* **11**, 2698–2712 (1998).
29. Song, I.-S., Byun, U.-Y., Hong, J. & Park, S.-H. Domain-size and top-height dependence in regional predictions for the Northeast Asia in spring. *Atmos. Sci. Lett.* **19**, e799 (2018).
30. Seo, G.-Y. et al. Hourly extreme rainfall projections over South Korea using convection permitting climate simulations. *npj Clim. Atmos. Sci.* **8**, 209 (2025).
31. Sinclair, V. A., Rantanen, M., Haapanala, P., Räisänen, J. & Järvinen, H. The characteristics and structure of extra-tropical cyclones in a warmer climate. *Weather Clim. Dynam.* **1**, 1–25 (2020).
32. Binder, H., Joos, H., Sprenger, M. & Wernli, H. Warm conveyor belts in present-day and future climate simulations – Part 2: role of potential vorticity production for cyclone intensification. *Weather Clim. Dynam.* **4**, 19–37 (2023).
33. Park, C., Son, S.-W. & Kim, H. Distinct features of atmospheric rivers in the early versus late East Asian summer monsoon and their impacts on monsoon rainfall. *J. Geophys. Res. Atmos.* **126**, e2020JD033537 (2021).
34. Kim, H.-R., Moon, M., Yun, J. & Ha, K.-J. Trends and spatio-temporal variability of summer mean and extreme precipitation across South Korea for 1973–2022. *Asia Pac. J. Atmos. Sci.* **59**, 385–398 (2023).
35. Kwon, Y. & Son, S.-W. East Asian atmospheric rivers are most hazardous in summer. *Weather Clim. Extremes* **44**, 100658 (2024).
36. Zhang, Z., Ralph, F. M. & Zheng, M. The relationship between extratropical cyclone strength and atmospheric river intensity and position. *Geophys. Res. Lett.* **46**, 1814–1823 (2019).
37. Trachte, K. Atmospheric moisture pathways to the highlands of the tropical andes: analyzing the effects of spectral nudging on different driving fields for regional climate modeling. *Atmosphere* **9**, 456 (2018).
38. Becker, E. et al. A high-resolution whole-atmosphere model with resolved gravity waves and specified large-scale dynamics in the troposphere and stratosphere. *J. Geophys. Res. Atmo.* **127**, e2021JD035018 (2022).
39. Uccellini, L. W. & Kocin, P. J. The interaction of jet streak circulations during heavy snow events along the East Coast of the United States. *Weather Forecast.* **2**, 289–308 (1987).
40. Yihui, D. & Chan, J. C. L. The East Asian summer monsoon: an overview. *Meteorol. Atmos. Phys.* **89**, 117–142 (2005).
41. Sinclair, V. A. & Catto, J. L. The relationship between extra-tropical cyclone intensity and precipitation in idealised current and future climates. *Weather Clim. Dynam.* **4**, 567–589 (2023).
42. Funatsu, B. M. & Waugh, D. W. Connections between Potential Vorticity Intrusions and Convection in the Eastern Tropical Pacific. *J. Atmos. Sci.* **65**, 987–1002 (2008).
43. Barnes, M. A., Ndarana, T., Sprenger, M. & Landman, W. A. Stratospheric intrusion depth and its effect on surface cyclogenetic forcing: an idealized potential vorticity (PV) inversion experiment. *Weather Clim. Dynam.* **3**, 1291–1309 (2022).
44. Škerlak, B., Sprenger, M., Pfahl, S., Tyrlis, E. & Wernli, H. Tropopause folds in ERA-Interim: Global climatology and relation to extreme weather events. *J. Geophys. Res. Atmos.* **120**, 4860–4877 (2015).
45. Bukenberger, M., Rüdisühli, S. & Schemm, S. Jet stream dynamics from a potential vorticity gradient perspective: the method and its application to a kilometre-scale simulation. *Q. J. R. Meteorol. Soc.* **149**, 2409–2432 (2023).
46. Horinouchi, T. & Hayashi, A. Meandering Subtropical jet and precipitation over summertime East Asia and the Northwestern Pacific. *J. Atmos. Sci.* **74**, 1233–1247 (2017).
47. Zhao, Y., Park, C. & Son, S.-W. Importance of diabatic heating for the eastward-moving heavy rainfall events along the Yangtze River, China. *J. Atmos. Sci.* **80**, 151–165 (2023).
48. Gill, A. E. *Atmosphere-ocean dynamics* (Elsevier Science, 1982).
49. Gómez, B. & Miguez-Macho, G. The impact of wave number selection and spin-up time in spectral nudging. *Q. J. R. Meteorol. Soc.* **143**, 1772–1786 (2017).
50. Li, T. & Fu, B. Tropical cyclogenesis associated with Rossby wave energy dispersion of a preexisting typhoon. Part I: satellite data analyses. *J. Atmos. Sci.* **63**, 1377–1389 (2006).

51. Prein, A. F. et al. A review on regional convection-permitting climate modeling: Demonstrations, prospects, and challenges. *Rev. Geophys.* **53**, 323–361 (2015).
52. Wang, X. et al. The sensitivity of simulated aerosol climatic impact to domain size using regional model (WRF-Chem v3.6). *Geosci. Model Dev.* **15**, 199–218 (2022).
53. Arthur, R. S., Lundquist, K. A., Mirocha, J. D. & Chow, F. K. Topographic effects on radiation in the WRF model with the immersed boundary method: implementation, validation, and application to complex terrain. *Monthly Weather Rev.* **146**, 3277–3292 (2018).
54. Liu, L., Ma, Y., Menenti, M., Zhang, X. & Ma, W. Evaluation of WRF modeling in relation to different land surface schemes and initial and boundary conditions: a snow event simulation over the Tibetan Plateau. *J. Geophys. Res. Atmos.* **124**, 209–226 (2019).
55. Verma, S., Panda, J. & Rath, S. S. Role of PBL and microphysical parameterizations during WRF simulated monsoonal heavy rainfall episodes over Mumbai. *Pure Appl. Geophys.* **178**, 3673–3702 (2021).
56. Prein, A. F., Ge, M., Valle, A. R., Wang, D. & Giangrande, S. E. Towards a Unified Setup to simulate mid-latitude and tropical mesoscale convective systems at kilometer-scales. *Earth Space Sci.* **9**, e2022EA002295 (2022).
57. Hiraga, Y. & Tahara, R. Sensitivity of localized heavy rainfall in Northern Japan to WRF physics parameterization schemes. *Atmos. Res.* **314**, 107802 (2025).
58. Yu, H., Prein, A. F., Qi, D. & Wang, K. Kilometer-scale multi-physics simulations of heavy precipitation events in Northeast China. *Clim. Dyn.* **62**, 9207–9231 (2024).
59. Hersbach, H. et al. The ERA5 global reanalysis. *Q. J. R. Meteorol. Soc.* **146**, 1999–2049 (2020).
60. Korea Meteorological Administration. High-resolution gridded data. *KMA Application Programmin Interface (API) Hub* https://apihub.kma.go.kr/apiList.do?seqApi=971 (2022).
61. Huffman, G. J. et al. GPM IMERG Final Precipitation L3 Half Hourly 0.1 degree x 0.1 degree V07. Greenbelt, MD, *Goddard Earth Sciences Data and Information Services Center (GES DISC)* https://disc.gsfc.nasa.gov/datasets/GPM_3IMERGHH_07/summary (2023).
62. Fosser, G., Kendon, E. J., Stephenson, D. & Tucker, S. Convection-permitting models offer promise of more certain extreme rainfall projections. *Geophys. Res. Lett.* **47**, e2020GL088151 (2020).
63. Lucas-Picher, P. et al. Convection -permitting modeling with regional climate models: Latest developments and next steps. *WIREs Clim. Change* **12**, e731 (2021).
64. Médus, E. et al. Characteristics of precipitation extremes over the Nordic region: added value of convection-permitting modeling. *Nat. Hazards Earth Syst. Sci.* **22**, 693–711 (2022).
65. Glisan, J. M., Gutowski, W. J., Cassano, J. J. & Higgins, M. E. Effects of spectral nudging in WRF on arctic temperature and precipitation simulations. *J. Clim.* **26**, 3985–3999 (2013).
66. Moon, J., Cha, D.-H., Lee, M. & Kim, J. Impact of spectral nudging on real-time tropical cyclone forecast. *J. Geophys. Res. Atmos.* **123**, 12,647–612,660 (2018).
67. Zhang, K. et al. Technical note: on the use of nudging for aerosol–climate model intercomparison studies. *Atmos. Chem. Phys.* **14**, 8631–8645 (2014).
68. Coll-Hidalgo, P., Gimeno-Sotelo, L., Fernández-Alvarez, J. C., Nieto, R. & Gimeno, L. North Atlantic extratropical cyclone tracks and lagrangian-derived moisture uptake dataset. *Sci. Data* **11**, 1258 (2024).
69. Nayak, M. A., Villarini, G. & Lavers, D. A. On the skill of numerical weather prediction models to forecast atmospheric rivers over the central United States. *Geophys. Res. Lett.* **41**, 4354–4362 (2014).
70. Pan, M. & Lu, M. A novel atmospheric river identification algorithm. *Water Resour. Res.* **55**, 6069–6087 (2019).
71. Guan, B. & Waliser, D. E. A regionally refined quarter-degree global atmospheric rivers database based on ERA5. *Sci. Data* **11**, 440 (2024).
72. Hersbach, H. et al. ERA5 hourly data on pressure levels from 1940 to present. *Copernicus Clim. Change Serv. (C3S) Clim. Data Store* https://doi.org/10.24381/cds.bd0915c6 (2023).

Acknowledgements

This study was funded by the KMA Research and Development Program under Grant RS-2024-00403386 and the Human Resource Program for Sustainable Environment in the 4th Industrial Revolution Society. Model simulation and data transfer are supported by the National Center for Meteorological Supercomputer of the Korea Meteorological Administration (KMA).

Author contributions

S.-K.M. conceived the study. D.K. and G.-Y.S. performed model experiments, conducted the analysis, and wrote the initial manuscript. All authors contributed to interpreting results and writing the manuscript.

Competing interests

The authors declare no competing financial interests.

Additional information

Supplementary information The online version contains supplementary material available at https://doi.org/10.1038/s41612-025-01224-4.

Correspondence and requests for materials should be addressed to Seung-Ki Min.